Lattice Boltzmann method for simulating the viscous flow in large distensible blood vessels

Haiping Fang,[1,2,3,*] Zuowei Wang,[2] Zhifang Lin,[2] Muren Liu[3]
[1]*Shanghai Institute of Nuclear Research, Chinese Academy of Sciences, P.O. Box 800-204, Shanghai 201800, China*
[2]*Department of Physics, Fudan University, Shanghai 200433, China*
[3]*Department of Physics, Guilin Normal University, Guilin, Guangxi, China*
(Received 28 December 2001; published 22 May 2002)

A lattice Boltzmann method for simulating the viscous flow in large distensible blood vessels is presented by introducing a boundary condition for elastic and moving boundaries. The mass conservation for the boundary condition is tested in detail. The viscous flow in elastic vessels is simulated with a pressure-radius relationship similar to that of the pulmonary blood vessels. The numerical results for steady flow agree with the analytical prediction to very high accuracy, and the simulation results for pulsatile flow are comparable with those of the aortic flows observed experimentally. The model is expected to find many applications for studying blood flows in large distensible arteries, especially in those suffering from atherosclerosis, stenosis, aneurysm, etc.

DOI: 10.1103/PhysRevE.65.051925 PACS number(s): 87.19.−j

I. INTRODUCTION

The study of the viscous fluid flow in large distensible blood vessels is an important area of practical interest [1,2]. It is well known that blood is a suspension of formed elements in plasma. The formed elements are the red cells, white cells, and platelets. The diameters of all these elements are usually less than 8 μm. In large arteries with diameters exceeding 100 μm, blood is usually regarded as effectively homogeneous, because the scale of the microstructure is so much smaller than that of the flow. Moreover, in these large arteries, blood is usually assumed to be Newtonian.

The artery walls are viscoelastic. The incremental Young's modulus affects the velocities of the artery walls, which is important in the study of blood flow in large arteries. However, the viscoelastic property of the artery walls makes the system too complex to be studied. In this paper, for the primary study of blood flow in large arteries, we assumed the arteries to be ideal elastic pipes.

The distensibility of the blood vessels adds considerable difficulty to the analysis of the flows in large blood vessels. Up to now, most theoretical works have been limited to linear theory and to models based on rigid tubes. In order to include the effect of nonlinearity and the elastic properties, numerical method plays a main role in this field. However, conventional methods for simulating viscous fluid flow in large blood vessels, including numerical integration of the Navier-Stokes equations, are particularly difficult to implement in complex and changeable geometries.

The lattice Boltzmann method (LBM) [3,4] has recently been proved competitive for studying the domain of fluid flow for various physical system. Based on the lattice gas automata (LGA) [5], the LBM inherited most of the advantages of the LGA and eliminated the excessive statistical noise and the lattice artifacts such as the lack of the Galilean invariance. In particular, the LBM is ideally suited for computation on parallel computers since most algorithms only depend on nearest-neighbor information. The LBM has been extended to simulate the flow through porous media [6,7], multiphase flow [8,9], suspension particles [10,11], chemically reacting flows [12], droplet deformation [13], and supersonic flow [14]. Recently the LBM has been applied to calculate photonic bond structure and defect modes in photonic band gap material [15]. In this paper, we extend the LBM for simulating the viscous flow in large distensible blood vessels. To this end, the moving impermeable boundary conditions with arbitrary geometry play an important role. Moreover, as the blood should not leak out of vessels, the boundary conditions adopted must satisfy mass conservation. Chen *et al.* [16] proposed an extrapolation scheme for LBM simulation in the viscous fluid system with complex geometry. Filippova and Hanel [17] suggested boundary-fitting conditions to achieve second-order accuracy on the complex boundary for steady-state flows. Ladd [10] was the first to apply the LBM to moving particles in the fluid by modifying the bounce-back rule to obtain a technique that is successful in many cases. Aidun *et al.* [11] extended the method to impermeable solid surfaces. They used the model to simulate the particle suspensions in fluid flow.

In this paper, a boundary condition at the moving wall boundary is presented and used to simulate the flows in distensible vessels. The mass conservation at the moving boundaries is tested in detail. Based on this model, the viscous flows in elastic vessels are simulated with a pressure-radius relationship similar to that of the pulmonary blood vessels [1]. The numerical results for steady flow are in excellent agreement with the analytical prediction, while those for pulsatile flow are comparable with those of the aortic flows observed experimentally [2]. These results, together with the simplicity and the ease of implementation of the model, suggest that our approach may be a promising tool for studying the blood flow in arteries, especially in those suffering from atherosclerosis, stenosis, or aneurysm.

The paper is organized as follows. In Sec. II we briefly describe the lattice Boltzmann method. Section III is devoted to a description of the boundary conditions. The mass conservation at the physical boundaries is considered in detail in Sec. IV. In Sec. V, the simulations on the steady and unsteady

*Mailing address: Department of Physics, Fudan University, Shanghai 200433, China. Email address: hpfang2000@yahoo.com

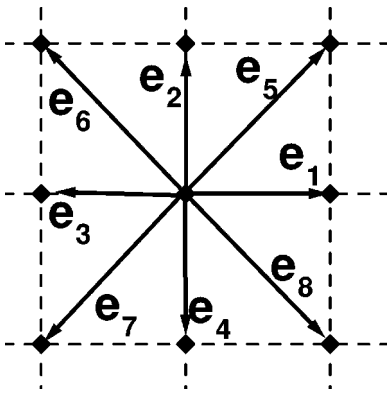

FIG. 1. Basic cell for the two-dimensional ''nine-speed'' lattice Boltzmann model.

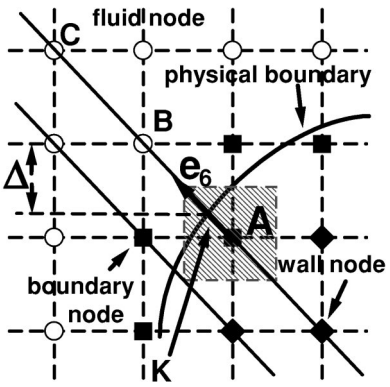

FIG. 2. Computational mesh and geometrical relation of solid boundaries.

flows, and their comparison with analytical predictions and experiment are presented. The conclusion and discussion are presented in Sec. VI.

II. THE LATTICE BOLTZMANN MODEL

In this paper we choose to work on a square lattice in two dimensions as shown in Fig. 1. Generalization to three dimensions is straightforward and the results for the three-dimensional case will be presented elsewhere. Let $f_i(\mathbf{x},t)$ be a non-negative real number describing the distribution function of the fluid density at site $\mathbf{x}$ at time t moving in direction $\mathbf{e}_i$. Here $\mathbf{e}_0=(0,0)$, $\mathbf{e}_i=(\cos\pi[i-1]/2,\sin\pi[i-1]/2)$, $i=1,2,3,4$, and $\mathbf{e}_i=(\cos\pi[2i-1]/4,\sin\pi[2i-1]/4)$, $i=5,6,7,8$ are the nine possible velocity vectors. The distribution functions evolve according to a Boltzmann equation that is discrete in both space and time [3,4],

$$f_i(\mathbf{x}+\mathbf{e}_i,t+1)-f_i(\mathbf{x},t)=-\frac{1}{\tau}(f_i-f_i^{eq}). \tag{1}$$

The density ρ and macroscopic velocity $\mathbf{u}$ are defined by

$$\rho=\sum_i f_i, \quad \rho\mathbf{u}=\sum_i f_i\mathbf{e}_i \tag{2}$$

and the equilibrium distribution functions f_i^{eq} are usually supposed to be dependent only on the local density ρ and flow velocity $\mathbf{u}$. A suitable choice reads [3,4]

$$f_i^{eq}=\rho\alpha_i\left[1+3\mathbf{e}_i\cdot\mathbf{u}+\frac{9}{2}(\mathbf{e}_i\cdot\mathbf{u})^2-\frac{3}{2}u^2\right], \tag{3}$$

where $\alpha_0=4/9$, $\alpha_1=\alpha_2=\alpha_3=\alpha_4=1/9$, and $\alpha_5=\alpha_6=\alpha_7=\alpha_8=1/36$. The macroscopic equations can be obtained by a Chapman-Enskog procedure [3,4]. They are the continuity equation

$$\partial_t\rho+\partial_\alpha(\rho u_\alpha)=0 \tag{4}$$

and the Navier-Stokes equations

$$\partial_t(\rho u_\alpha)+\partial_\beta(\rho u_\alpha u_\beta)=\partial_\alpha p+\nu\partial_\beta[\rho(\partial_\alpha u_\beta+\partial_\beta u_\alpha)], \tag{5}$$

where p and ν are the pressure and the viscosity, respectively, defined by the equations $p=c_s^2\rho$ with $c_s^2=1/3$ and $\nu=(2\tau-1)/6$.

III. THE BOUNDARY CONDITIONS

A. Boundary conditions for stationary boundaries

For clarity of the following description, let us first define three types of nodes: boundary nodes, fluid nodes, and wall nodes. In Fig. 2 we show an example, where the heavy solid line is a physical boundary, under which is a wall. Associate with each lattice node a *square* of unit sides centered at the node, as shown in Fig. 2 by the shaded part. A node is called *a boundary node* if any physical boundary crosses its *square* (see, e.g., node *A* in Fig. 2). In Fig. 2 the boundary node is represented by a filled square. A node is called a wall node (fluid node) if its associated square is wholly inside the impermeable wall (fluid domain), as shown by a filled diamond (open circle) [18].

It is clear that only a part of the square of the boundary node is filled with fluid, so that the real fluid density at the boundary node is significantly less than those at its neighboring fluid nodes. In fact, for any boundary node, only the distribution function in the direction $\mathbf{e}_i$ pointing toward a fluid node is *relevant*, which will be used in the streaming step, while the distribution function in the direction $\mathbf{e}_i$ pointing toward a boundary node or wall node is *irrelevant*. Similar to what was proposed by Chen *et al.* [16], the relevant distribution functions at these boundary nodes are obtained by extrapolation before each streaming. However, the present scheme includes two steps: the extrapolation of the nonequilibrium part of the distribution function, and the extrapolation of the *temporary* density and *temporary* velocity (to be defined below), based on which the equilibrium part of the distribution function is specified. To be more specific, let us take the boundary node marked by *A* in Fig. 2 as an example. In order to obtain $f_6(\mathbf{x}_B)$ by streaming, $f_6(\mathbf{x}_A)$ should be determined. Denote

$$f_6(\mathbf{x}_A)=f_6^{eq}(\mathbf{x}_A)+f_6^{neq}(\mathbf{x}_A), \tag{6}$$

where $f_6^{eq}(\mathbf{x}_A)$ and $f_6^{neq}(\mathbf{x}_A)$ are the equilibrium and nonequilibrium parts of the distribution function $f_6(\mathbf{x}_A)$. We assume that

$$f_6^{neq}(\mathbf{x}_A) = 2f_6^{neq}(\mathbf{x}_B) - f_6^{neq}(\mathbf{x}_C). \tag{7}$$

This extrapolation scheme guarantees first-order numerical accuracy for f_6^{neq}. For example, assume that the spatial increment is dx. Using Taylor's expansion we know that $f_6^{neq}(\mathbf{x}_B) = [f_6^{neq}(\mathbf{x}_A) + f_6^{neq}(\mathbf{x}_C)]/2) + O(dx^2)$ [assuming $f_6^{neq}(\mathbf{x}_A)$ and $f_6^{neq}(\mathbf{x}_C)$ are known], or $f_6^{neq}(\mathbf{x}_A) = 2f_6^{neq}(\mathbf{x}_B) - f_6^{neq}(\mathbf{x}_C) + O(dx^2)$ [assuming $f_6^{neq}(\mathbf{x}_B)$ and $f_6^{neq}(\mathbf{x}_C)$ are known], leading to a first-order accuracy approximation of the nonequilibrium part of the unknown distribution function at a boundary node [16]. As the nonequilibrium part is the first-order small quantity in the Chapman-Enskog procedure, the error caused by Eq. (7) in $f_6(\mathbf{x}_A)$ is of third order.

The equilibrium part $f_6^{eq}(\mathbf{x}_A)$ is calculated based on Eq. (3) with the *temporary* density ρ_A and velocity $\mathbf{v}_A$. The latters are obtained by the following extrapolation and interpolation, respectively:

$$\rho_A = 2\rho_B - \rho_C, \tag{8}$$

$$\mathbf{v}_A = \frac{\mathbf{v}_K + (\Delta - 1)\mathbf{v}_B}{\Delta}, \quad 0.5 \leqslant \Delta < 1.5, \tag{9}$$

where ρ_B and ρ_C are the well-defined densities at the fluid nodes B and C, Δ is the vertical distance from the point K on the physical boundary to the node B shown in Fig. 2, and $\mathbf{v}_K$ and $\mathbf{v}_B$ are the fluid velocities at K and B, respectively. As $\mathbf{v}_K$ is the velocity of the fluid at K, it *can be nonzero* while the physical boundary is stationary if the boundary is permeable. With $f_6(\mathbf{x}_A)$, the streaming from the boundary node A to the fluid node B can be carried out like that between the fluid nodes. It should be noted that although Eq. (9) is the same as that in the paper of Filippova and Hanel [17], the range of Δ is $0.5 \leqslant \Delta < 1.5$, which avoids the singularity point of $\Delta = 0$.

The above procedure [Eqs. (6)–(9)] is applied to each relevant direction $\mathbf{e}_i$ of a boundary node at $\mathbf{x}$ to obtain $f_i(\mathbf{x})$ for streaming, while $f_i(\mathbf{x})$ in the irrelevant direction $\mathbf{e}_i$ is undefined. The macroscopic densities and velocities at the boundary nodes are also undefined at this stage, while the *temporary* density and velocities in Eqs. (8) and (9) are introduced solely for the calculation of the equilibrium distribution function in the direction $\mathbf{e}_i$.

B. Numerical demonstration of the accuracy of the boundary condition

The Poiseuille flow in an inclined tube shown in Fig. 3 with the velocity of the fluid at the tube boundary $v_k = 0$ provides a good benchmark for testing the boundary condition, since its boundary is not flat, while analytical results are available that make the comparison to high accuracy possible. The analytical solution for the velocity profile is known and given by

$$u_j = u_0\left(1 - \frac{j^2}{d^2}\right), \tag{10}$$

where u_j is the component of the velocity vector along the flow direction at a distance j from the centerline of the tube,

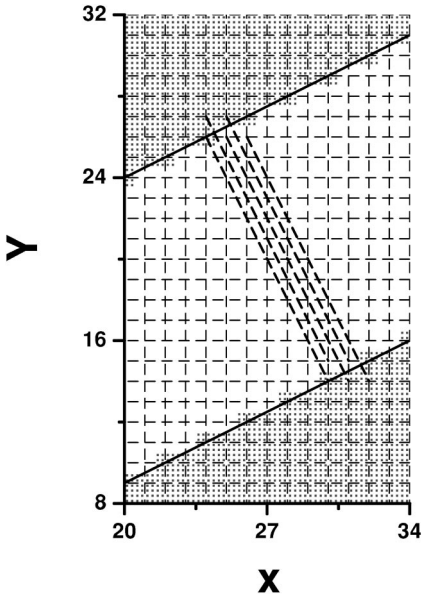

FIG. 3. Part of an inclined tube for the inclination angle $\theta = \tan^{-1}(1/2)$. The solid lines are the physical boundaries of the tube. If the halfway bounce-back rule is applied, the unshaded part represents the fluid domain. The heavy dashed lines are the reference lines for measuring the velocities.

d is the radius of the tube, and u_0 is the maximal velocity, which depends on the pressure difference Δp between the inlet and outlet. The relative error at location j, ϵ_j^{rel}, is defined as

$$\epsilon_j^{rel} = \left|\frac{u_j - \overline{u_j}}{u_j}\right|, \tag{11}$$

where $\overline{u_j}$ is the simulated velocity at location j. In order to minimize the error due to the inlet and outlet, we consider the inclined tube with $\theta = \tan^{-1}(k/l)$, where k is a nonnegative integer, l is a positive integer so that all the nodes at $\mathbf{x} + nl\mathbf{e}_1 + nk\mathbf{e}_2$, with n being an arbitrary integer, share the same distance from the centerline and velocity for the analytical solution (10). Unlike a flat tube along the x direction, where all the nodes at the inlet (outlet) share a same x value, for an inclined tube the inlet (outlet) is like the left-most heavy dash line in Fig. 3. Explicitly, the nodes at the inlet (outlet) of this inclined tube locate on a line $y - y_0 = -(l/k)x - x_0$, where $\mathbf{x} = (x_0, y_0)$ is a node at the inlet (outlet). Without loss of generality, we assume $l \geqslant k$. We set

$$f_i(\mathbf{x})/f_0(\mathbf{x}) = f_i(\mathbf{x} + l\mathbf{e}_1 + k\mathbf{e}_2)/f_0(\mathbf{x} + l\mathbf{e}_1 + k\mathbf{e}_2)$$

when $\mathbf{x}$ is a fluid node at the inlet,

$$f_i(\mathbf{x})/f_0(\mathbf{x}) = f_i(\mathbf{x} - l\mathbf{e}_1 - k\mathbf{e}_2)/f_0(\mathbf{x} - l\mathbf{e}_1 - k\mathbf{e}_2)$$

with $\mathbf{x}$ being a fluid node at the outlet

for $i = 1,2,\ldots,8$, while the density at the inlet (outlet) is fixed. Since the node at $\mathbf{x}$ at the inlet (outlet) and the node at $\mathbf{x} + l\mathbf{e}_1 + k\mathbf{e}_2$ ($\mathbf{x} - l\mathbf{e}_1 - k\mathbf{e}_2$) in the fluid domain share the same distance from the centerline, these assumptions guaran-

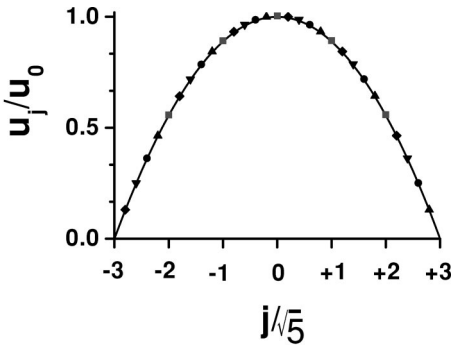

FIG. 4. The normalized velocity profile obtained by applying the boundary conditions proposed in this paper. j is the distance from a node to the centerline of the tube with the signs + and − denoting the node above or below the centerline, respectively. The solid line is the analytical result. The filled squares, circles, diamonds, up triangles, and the down triangles are the simulation results for the nodes on the heavy dashed lines shown in Fig. 3, from left to right, respectively.

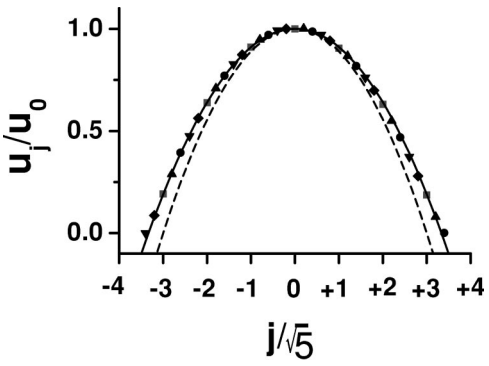

FIG. 5. The same as Fig. 4 except that the halfway bounce-back rule is applied. The solid line is the best fit of the simulation results. The dashed line is the same as the solid line in Fig. 4, which is the expected analytical prediction.

tee that they share the same velocity, satisfying the analytical results (10). Moreover, the distribution functions in some directions at the nodes near the inlet (or the outlet) cannot be determined in the streaming step for an inclined tube. An example is the distribution function from the left side of the nodes on the second left-most heavy dashed line in Fig. 3 if we assume that the left-most heavy dashed line is the inlet. In the present simulation, they can also be determined by the above equations. In the present paper, we only show the results for $2k=l=2$.

Initially, the distribution functions at all the fluid nodes, including those at the inlet and outlet, are assumed to be the equilibrium distribution functions with zero velocity and one unit density. In the first 1000 time steps, the density at the inlet (outlet) increases (decreases) linearly up to a fixed density ρ_{in} (ρ_{out}). After 10 000 time steps, the system is stable enough for analysis. In Fig. 4 we show the velocity profile for the fluid nodes on the heavy dashed lines shown in Fig. 3 with the present boundary condition for $d=3\sqrt{5}$ and $\tau=1$. The simulation results are quite consistent with the analytical results. For comparison, the simulation results with the halfway bounce-back rule [19] are shown in Fig. 5. It is clear that the present boundary condition greatly improves the simulation results. Moreover, the real boundary, corresponding to the zero velocity, cannot be predetermined if the halfway bounce-back rule is applied for a nonflat boundary.

The maximal relative error ϵ_{max}^{rel}, which is the maximal value of ϵ_i^{rel}, and the global error ϵ_g in velocity field of simulation against analytical results are, respectively, defined as

$$\epsilon_{max}^{rel}=\max\{\epsilon_i^{rel}\},$$

$$\epsilon_g=\sqrt{\frac{\sum_i \|\mathbf{u}(\mathbf{x}_i,t)-\overline{\mathbf{u}}(\mathbf{x}_i,t)\|^2}{\sum_i \mathbf{u}(\mathbf{x}_i,t)^2}}, \qquad (12)$$

where i runs over all fluid nodes on the dashed lines in Fig. 3. ϵ_{max}^{rel} and ϵ_g for different width d of the tube are presented in Fig. 6. Both ϵ_g and ϵ_{max}^{rel} are very small and less than 1% even for $d=3$. In all the simulations, u_0 is fixed to 0.02.

We further consider the case with the fluid at the tube wall having a fixed velocity $\mathbf{v}_k=(u_\parallel,u_\perp)$, where $u_\parallel$ and $u_\perp$ are the velocity components parallel and perpendicular to the tube, respectively. Some simulation results are in order. Now the analytical results of the velocity of the fluid should be the vector sum of the velocity $\mathbf{v}_k$ and Eq. (10).

(1) Numerically we find that the simulations achieve machine accuracy if $\Delta p=0$.

(2) When $\Delta p\neq 0$, $u_\parallel\neq 0$, and $u_\perp=0$, corresponding to nonslip of the fluid at the boundary when the tube is moving along its axis, the simulation results show that the existence of non-zero $u_\parallel$ does not degrade the accuracy.

(3) When $\Delta p\neq 0$, $u_\parallel=0$, and $u_\perp\neq 0$, corresponding to leakage of the fluid out of the tube or a distensible impermeable tube, the error is relative large and decreases as $u_\perp/u_0$ decreases, where u_0 is the maximal velocity in the tube for the case with the same pressure drop Δp and $u_\perp=u_\parallel=0$ [see Eq. (10)]. The maximal relative error and the global error are shown in Fig. 7. ϵ_g decreases linearly as $u_\perp/u_0$. For most of the cases, such as the blood flow in elastic (blood) vessels, $u_\perp/u_0$ is very small and our scheme achieves sufficient accuracy.

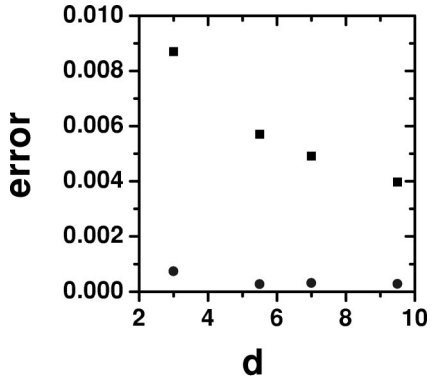

FIG. 6. The maximal relative error ϵ_{max}^{rel} (filled squares) and the global error ϵ_g (filled circles) for different widths d.

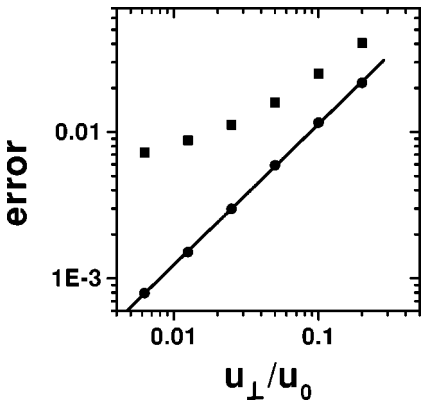

FIG. 7. The maximal relative error ϵ_{max}^{rel} (filled squares) and the global error ϵ_g (filled circles) for different vertical velocities of the boundaries. The solid line is a linear fit of ϵ_g, which shows that ϵ_g decreases as $u_\perp/u_0$.

(4) When $\Delta p \neq 0$, $u_\parallel \neq 0$, and $u_\perp \neq 0$, the accuracy of the simulation is almost the same as case (3).

Although the above numerical results are obtained for $\tau = 1$ and $u_0 = 0.02$, numerically we find that the simulation achieves similar accuracy for $0.75 \leqslant \tau \leqslant 2$ and $u_0 \leqslant 0.2$. Thus, the scheme is a good candidate for the boundary conditions for stationary boundaries. The boundary condition for the nonstationary boundaries can be considered based on this scheme.

C. Boundary condition for nonstationary boundaries

If the physical boundary has nonzero vertical velocity, some boundary nodes will change into fluid nodes and vice versa. As described above, the distribution functions in irrelevant directions at any boundary node are undefined. However, once a boundary node becomes a fluid node, all the distribution functions should be well defined. In our simulation scheme, at the time a boundary node turns into a fluid node, the distribution functions for this boundary node are assumed to be the average of the extrapolated values from a *second-order extrapolation scheme* of all the possible directions. This is consistent with the above boundary condition based on interpolation and extrapolation. For example, when the physical boundary shown in Fig. 8 moves downward, the node *D* will become a fluid node. There are four directions $\mathbf{e}_2, \mathbf{e}_3, \mathbf{e}_5, \mathbf{e}_6$ pointing toward fluid nodes. The distribution functions at *D* are obtained as

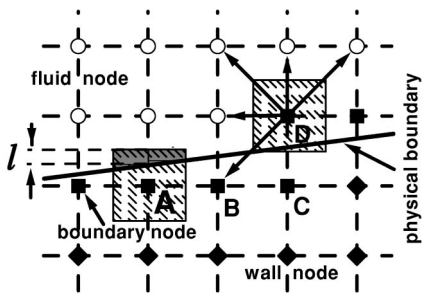

FIG. 8. The relation between the boundary nodes and fluid nodes near a nonflat physical boundary.

$$f_i(\mathbf{x}_D) = \frac{\sum_{j=2,3,5,6} \{2f_i(\mathbf{x}_D + \mathbf{e}_j) - f_i(\mathbf{x}_D + 2\mathbf{e}_j)\}}{4}$$

$$\text{for } i = 0,1,\ldots,8. \quad (13)$$

IV. TESTING THE MASS CONSERVATION OF THE BOUNDARY CONDITION

In this section we will show that the boundary condition described in the above section can be applied to study the viscous flow with moving and impermeable boundaries.

A. Necessary conditions for a boundary condition for impermeable boundaries

As the node *A* shown in Fig. 8, only a (shaded) part of the *square* of a boundary node falls in the fluid domain. As a result, the *real* fluid mass m_b inside the square of the boundary node should be considerably smaller than that in the neighbor fluid node. If we assume, as in most cases of the LBM simulations, that the fluid density in the simulation domain is (approximately) constant, ρ_0, we have

$$m_b = \rho_0 S,$$

where *S* is the area of the shaded part of the square of a boundary node. In other words, because the area of the square associated with any node is always unity, we may consider that the fluid density at the boundary node is

$$\rho = m_b = \rho_0 S. \quad (14)$$

We emphasize that the *capacity* of the boundary node *A* for fluid particles is $\rho_0 S$. The shaded area of the node *A* can only be filled with $\rho_0 S$ fluid particles, while there is no fluid particle in the other part of the node *A*.

If the inclined angle of the boundary is small, as in the case of node *A*, the fluid density at the boundary node can be approximated by

$$\rho = \rho_0 S = \rho_0 l, \quad (15)$$

where *l* is the length shown in Fig. 8, since all squares are of unit sides.

In the LBM simulation, *l* and ρ are obtained *separately*. *l* is found based on the position of the physical boundary, while ρ, which is the fluid mass accumulated or leftover at the boundary, is determined by the fluid particle transfer between the partly filled boundary node and its neighboring fluid nodes in a series of streaming steps. We can, therefore, define a quantity

$$C(l,\rho) = (\rho_0 l - \rho)/\rho_0 = l - \rho/\rho_0$$

to characterize the degree of mass conservation at the boundary. Obviously, $C(l,\rho) = 0$ corresponds to Eq. (15). There is mass conservation at the boundary since the shaded part is completely filled with $\rho_0 l$ fluid particles without any free space and extra fluid particles left. If $C(l,\rho) < 0$, then ρ

$>\rho_0 l$ and the extra fluid $\rho-\rho_0 l$ is believed to have entered the wall, since the capacity of the boundary node for fluid particles is only $\rho_0 l$, which can stay in the shaded part of the *square* of the boundary node. Similarly, when $C(l,\rho)>0$, $\rho<\rho_0 l$ and the difference $\rho_0 l-\rho$ is regarded as fluid particles coming from the wall since the shaded part of the *square* of the boundary node must be filled with $\rho_0 l$ fluid particles. As a result, the wall behaves in some sense like a fluid reservoir, or physically, the boundary should be permeable. An impermeable boundary requires that the boundary conditions should yield (nearly) vanishing $C(l,\rho)$.

In the following three subsections we will show that the present boundary condition leads to a (nearly) vanishing $C(l,\rho)$. So it can be applied to the impermeable boundaries.

B. Analysis and simulation of the viscous flow in a channel with impermeable flat boundaries

Consider a channel with a flat wall moving with a constant velocity $\mathbf{u}=(u_x,u_y)=(u,-v)$, where u and $-v$ are the parallel and vertical components, respectively. Without loss of generality, we assume $v>0$. After the system becomes stable, all the fluid nodes share the *same and time-independent* distribution functions f_i, $i=0,1,2,\ldots,8$ and density ρ_0. The relevant distribution functions of the boundary nodes are also the same as those of the fluid nodes.

Let us consider a boundary node A at $\mathbf{x}_A$ of a bottom boundary (see, e.g., the node A shown in Fig. 8). In the streaming step, the distribution function $f_4(\mathbf{x}_A-\mathbf{e}_4)$, $f_7(\mathbf{x}_A-\mathbf{e}_7)$, and $f_8(\mathbf{x}_A-\mathbf{e}_8)$ will propagate to the node A. The node A thus receives fluid $f_4(\mathbf{x}_A-\mathbf{e}_4)+f_7(\mathbf{x}_A-\mathbf{e}_7)+f_8(\mathbf{x}_A-\mathbf{e}_8)$ in the streaming step. On the other hand, the fluid distribution functions $f_2(\mathbf{x}_A)$, $f_5(\mathbf{x}_A)$, and $f_6(\mathbf{x}_A)$ will leave the node A and propagate to the nodes at $\mathbf{x}_A+\mathbf{e}_2$, $\mathbf{x}_A+\mathbf{e}_5$, and $\mathbf{x}_A+\mathbf{e}_6$, respectively. The node A loses fluid $f_2(\mathbf{x}_A)+f_5(\mathbf{x}_A)+f_6(\mathbf{x}_A)$ in the streaming step. The increment of the fluid density at the boundary node A in a the streaming step is, therefore,

$$\delta\rho=[f_4(\mathbf{x}_A-\mathbf{e}_4)+f_7(\mathbf{x}_A-\mathbf{e}_7)+f_8(\mathbf{x}_A-\mathbf{e}_8)]-[f_2(\mathbf{x}_A)+f_5(\mathbf{x}_A)+f_6(\mathbf{x}_A)].$$

Recalling that all the fluid nodes and the relevant directions of the boundary nodes share the same and time-independent distribution functions $f_i(\mathbf{x})$ for any i, one gets

$$\delta\rho=f_4+f_7+f_8-f_2-f_5-f_6=-\rho_0 u_y=\rho_0 v. \quad (16)$$

In the time interval $[t_0,t_1]$, the increment of the density ρ is $v(t_1-t_0)$. Let t_0 be the time when wall node at $\mathbf{x}$ becomes a boundary node and t_1 the time when the boundary node turns to a fluid node, i.e.,

$$\text{a wall node} \xrightarrow{\text{at } t_0} \text{a boundary node} \xrightarrow{\text{at } t_1} \text{a fluid node}. \quad (17)$$

Then one has the fluid density $\rho(\mathbf{x},t_0)=0$ and $\Sigma_{t=t_0}^{t_1} v\Delta t=1$. Here $\Delta t=1$ is the time step. As a result, the density at the node at t_1 reads

$$\rho(\mathbf{x},t_1)=\sum_{t=t_0}^{t_1}\delta\rho\Delta t=\sum_{t=t_0}^{t_1}\rho_0 v\Delta t=\rho_0\sum_{t=t_0}^{t_1} v\Delta t=\rho_0. \quad (18)$$

This new fluid node, therefore, has the same density as other fluid nodes, yielding no perturbation when the boundary node becomes a fluid node. Moreover, at time t_a with $t_0<t_a<t_1$, $l=v(t_a-t_0)$, and $\rho=\rho_0 v(t_a-t_0)$, we get

$$C(l,\rho)=l-\rho/\rho_0=0.$$

A similar result can be obtained for the process

$$\text{a fluid node}\rightarrow\text{a boundary node}\rightarrow\text{a wall node} \quad (19)$$

as well. We verify this by numerical simulation. The simulation results achieve machine accuracy.

C. Simulation of the viscous flow in a channel with impermeable nonflat boundaries

If the channel considered above has nonflat walls as shown in Fig. 8, we may have to consider the boundary condition for the nodes *B*, *C*, and *D*. The streaming between the boundary nodes *B* and *D* will also be considered to guarantee that the density increment on the node *B* behaves the same as the other boundary nodes on the flat boundary. The distributions functions for such streaming are obtained by the average of the extrapolated values of all the possible directions. For example, there are two directions, $\mathbf{e}_2$ and $\mathbf{e}_6$, for the node *B* with the directions pointing toward fluid nodes. The distribution function $f_5(\mathbf{x}_B)$ is enforced by

$$f_5(\mathbf{x}_B)=\frac{\sum_{j=2,6} f_5(\mathbf{x}_B+\mathbf{e}_j)}{2}. \quad (20)$$

We can get the same result [Eq. (18)] in a way similar to that shown in the above section.

The cases for nodes *C* and *D* are completely different. The increment of the fluid density at the node *D* in each (streaming) time step is

$$\begin{aligned}\delta\rho_D&=f_4(\mathbf{x}_D-\mathbf{e}_4)+f_7(\mathbf{x}_D-\mathbf{e}_7)+f_8(\mathbf{x}_D-\mathbf{e}_8)+f_1(\mathbf{x}_D-\mathbf{e}_1)\\&\quad+f_5(\mathbf{x}_D-\mathbf{e}_5)-f_2(\mathbf{x}_D)-f_5(\mathbf{x}_D)-f_6(\mathbf{x}_D)-f_3(\mathbf{x}_D)\\&\quad-f_7(\mathbf{x}_D)\\&=f_4+f_7+f_8+f_1+f_5-f_2-f_5-f_6-f_3-f_7=f_4+f_1\\&\quad+f_8-f_2-f_3-f_6. \quad (21)\end{aligned}$$

The increment of the fluid density at the node *C* in each (streaming) time step is

$$\delta\rho_C=f_8(\mathbf{x}_C-\mathbf{e}_8)-f_6(\mathbf{x}_C)=f_8-f_6. \quad (22)$$

The total increment of the fluid density at both the nodes *C* and *D* in each (streaming) time step is

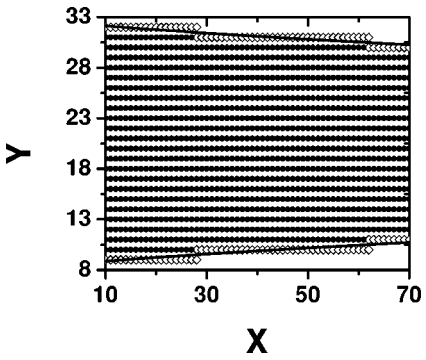

FIG. 9. A channel with nonflat boundaries. The boundary nodes and the fluid nodes are represented by open diamonds and filled circles, respectively.

$$\begin{aligned}\delta\rho &= \delta\rho_C + \delta\rho_D \\ &= f_4 + f_7 + f_8 - f_2 - f_5 - f_6 + f_1 + f_5 + f_8 - f_3 - f_6 - f_7 \\ &= \rho_0(u_x - u_y) \\ &= \rho_0(u + v). \end{aligned} \tag{23}$$

If we set $u=0$ and take $\delta\rho$ as the total increment of the density at the node D in each time step, we can get Eq. (16) and we are in the same situation as the flat boundary. (The case for $u\neq 0$ will be considered elsewhere, in which we may have to consider the streaming of the distribution functions between the neighbor boundary nodes). We verify this with a numerical simulation of the tube shown in Fig. 9. The simulation also achieves machine accuracy.

In the case of varying v, we cannot get the analytical result as Eq. (23), since the distribution function is different at different fluid nodes and different times. However, numerical simulations show that $|C(l,\rho)|$ is very small. We have performed a simulation of the viscous fluid flow in the channel shown in Fig. 9 for 2000 time steps with $v = v_0 \sin(\omega t)$, where $v_0 = 0.004$ and $\omega = 2\pi/T$ with the period $T=1000$. The distribution of $C(l,\rho)$ is shown Fig. 10 for all boundary nodes, corresponding to different values of l; see open diamonds in Fig. 9. The maximal absolute error for $|C(l,\rho)|$ is 0.0035. In the simulation, the densities at the nodes at the inlet and outlet are fixed to be $\rho_0 = 1$. The error comes from the deviation of the density from ρ_0, which results from the *time-dependent* velocity v. In Fig. 11, we show the densities at the nodes at $x=40$ with respect to y for different times t. The densities at these nodes oscillate with $\sin(\omega t)$. Moreover, we can see that it seems that $|C(l,\rho)|$ shown in Fig. 10 depends on l single valuedly except at a few points above the curve. Since the channel is nonflat, l may be different for different boundary nodes. On the other hand, different nodes may share the same value of l. The boundary nodes share the same l, while the values of $C(l,\rho)$ are different, resulting in the multivalued results. A careful examination shows that these points come from the data close to the inlet and outlet. We believe that the error can be reduced if we can apply a lattice Boltzmann method with nearly constant density [20].

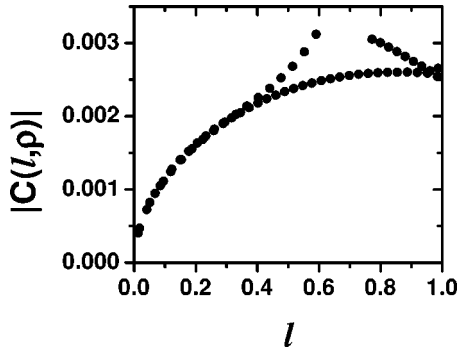

FIG. 10. $|C(l,\rho)|$ vs l in the channel with nonflat boundaries shown in Fig. 9 with the densities $\rho_0 = 1$ at the inlet and outlet. The channel moves perpendicular to the channel with velocity $(u_x, u_y) = [0, 0.004\sin(2\pi t/1000)]$.

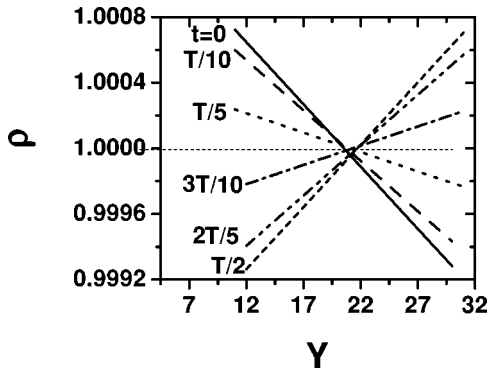

FIG. 11. The densities at the nodes at $x=40$ with respect to y for different time t. T is the period of oscillation.

D. Simulation on the viscous flow in a channel with density difference between inlet and outlet

The pressure is proportional to the density in the conventional lattice Boltzmann models. In most of the cases we have to consider viscous flow with pressure gradient, so that the density is different at different fluid nodes and different times. For these systems, Eqs. (14) and (15) and the quantity $C(l,\rho)$ will have to be modified as

$$\rho = \rho_n S, \tag{24}$$

$$\rho = \rho_n l, \tag{25}$$

and

$$C(l,\rho) = l - \rho/\rho_n,$$

where ρ_n is determined by the densities of the fluid nodes nearby. A suitable choice is that ρ_n is the average of the extrapolated values from a *second-order extrapolation scheme* of all the possible directions, as shown in Eq. (20). The absolute value of $C(l,\rho)$ is much larger in those cases. In Fig. 12 we show the simulation results for the viscous flow in the same channel shown in Fig. 9 for 2000 time steps with $v=0.003$ and $v = v_0 \sin(\omega t)$, respectively. Here $v_0 = 0.004$ and $\omega = 2\pi/1000$. The densities at the nodes on the inlet and outlet are fixed to be 0.9918 and 1.0066, respec-

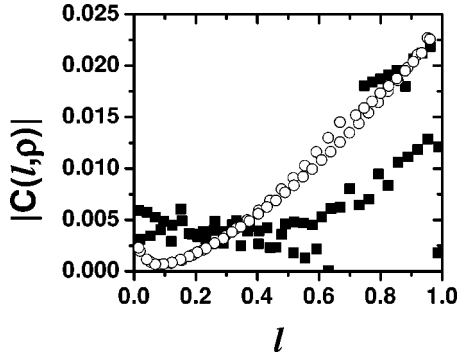

FIG. 12. $|C(l,\rho)|$ vs l in the channel with nonflat boundaries shown in Fig. 9 with the densities at the nodes on the inlet and outlet of 0.9918 and 1.0066, corresponding to the maximal velocity component along the channel at the outlet being 0.0368. The channel wall moves perpendicular to the channel with velocity $(u_x,u_y)=[0,0.004\sin(2\pi t/1000)]$ (open circles) and $(u_x,u_y)=(0,0.003)$ (filled squares), respectively.

tively, corresponding to the maximal velocity component along the channel at the outlet being 0.0368. $|C(l,\rho)|$ is less than 0.02 and 0.05 for the constant and varying velocities, respectively.

E. Simulation of the viscous flow in a channel with elastic boundaries

Initially the tube has a constant radius $a_0=9.5$, and the density decreases linearly from 1.0190 to 1.0034 along the channel. For our LBM simulation, the channel is 59 lattice units in length so that each (upper or lower) boundary is composed of 59 small segments with unit length. A linear compliance force $-\alpha\Delta y$ is applied on the segment if its displacement from the initial location is Δy. The mass for each segment is 500 and $\alpha=0.002$. The pressure p_s at each segment of the physical boundary is obtained by linear extrapolation. p_s-p_0 determines the net hydrodynamic force acting on this segment, where $p_0=1/3$. The sum of the net hydrodynamic force and the compliance force gives its velocity and its displacement from the equilibrium location by Newtonian dynamics. After 800 time steps, we get the channel shown in Fig. 9, $|C(l,\rho)|$ are shown in Fig. 13. $|C(l,\rho)|$ is less than 0.02.

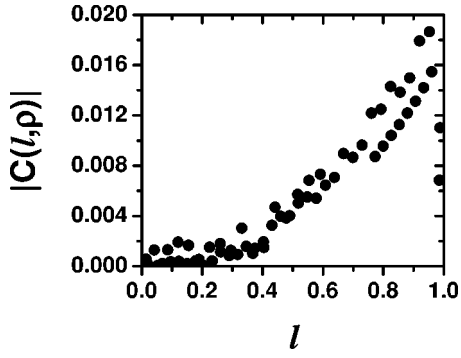

FIG. 13. $|C(l,\rho)|$ vs l in the channel with elastic boundaries.

The above discussion shows that the boundary condition can be applied to simulate the viscous flow with moving and impermeable boundaries. *The errors mainly result from the compressibility of the lattice Boltzmann model*, as had been discussed in Sec. IV C. If there is an incompressible model with explicit constant density while the pressure deviation is allowed [20], Eqs. (16) and (23) are guaranteed at least to first-order accuracy for the flat and nonflat boundaries, respectively. In the simulation of the viscous flow in the large blood vessels, the longitudinal movement is usually neglected [2]. Consequently, there is approximate mass conservation for both the flat and nonflat boundaries with an arbitrary velocity in the present scheme.

V. NUMERICAL SIMULATIONS OF THE VISCOUS FLOW IN DISTENSIBLE TUBES

A. Steady flow in an elastic tube

We perform simulation of a long and thin plane elastic pipe with length L. The pressure $p(x)$ to width $a(x)$ relationship is assumed to be linear

$$p(x)-p_0=\alpha(a(x)-a_0), \tag{26}$$

where a_0 is the width when the pressure inside is fixed to p_0 and α is a compliance constant. In the three-dimensional case with a being the tube radius, Eq. (26) is a good representation of the pulmonary blood vessels [1]. Denoting the pressure at the inlet and outlet by $p(0)$ and $p(L)$, respectively, we assume $p(0)>p(L)$. Since the pipe is long and thin, that is, $L\ll a$, and the pipe is smooth under deformation, the velocity can be approximated by that of the plane Poiseuille flow [1]. Denoting by $u(x,y)$ the longitudinal velocity of the flow in the tube at (x,y),

$$u(x,y)=u_0(x)\left[1-\frac{4y^2}{a^2(x)}\right],$$

where y is the distance from the centerline,

$$u_0(x)=-\frac{\partial p(x)}{\partial x}\frac{a^2(x)}{8\nu}$$

is the velocity at the centerline. The volume-flow rate at x is

$$Q(x)=\int_{-R}^{R}u(x,y)dy=\frac{2}{3}u_0(x)a(x)=-\frac{a^3(x)}{12\nu}\frac{\partial p(x)}{\partial x}.$$

From Eq. (26),

$$\frac{\partial p(x)}{\partial x}=\alpha\frac{da(x)}{dx}.$$

Consequently

$$Q=-\frac{\alpha a^3(x)}{12\nu}\frac{da(x)}{dx}.$$

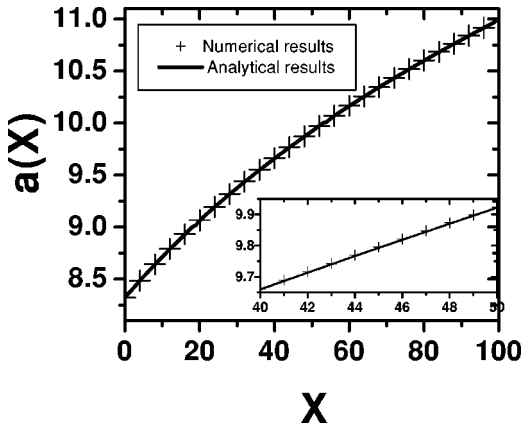

FIG. 14. The analytical prediction (−) and numerical simulation results (+) of the width $a(x)$ of an elastic pipe along the channel.

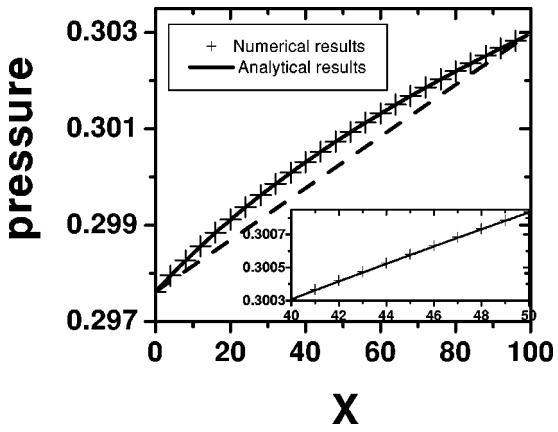

FIG. 15. The analytical prediction (−) and numerical simulation results (+) of the pressure $p(x)$ in the same elastic pipe of Fig. 14. The dashed line is a linear connection between the beginning and ending points serving as a guide to eyes, which should be the result for a rigid pipe.

In a stationary, nonpermeable tube, Q is constant through the length of the tube. Integrating this equation, we obtain, for steady flow, a theoretical formula for the width $a(x)$ and the pressure $p(x)$,

$$a^4(x)-a^4(0)=Bx, \quad B=-48\nu Q/\alpha, \tag{27}$$

$$\left[a_0+\frac{p(x)-p_0}{\alpha}\right]^4-\left[a_0+\frac{p(0)-p_0}{\alpha}\right]^4=Bx, \tag{28}$$

where Q is the volume-flow rate, which is constant throughout the pipe in a stationary, nonpermeable pipe.

For our LBM simulation, the pipe is 100 lattice units in length so that each (upper or lower) boundary is composed of 100 small segments with unit length. Each unit is assumed to obey Hooke's law, i.e., a linear compliance force $-\alpha\Delta y$ is applied on the segment if the displacement from the equilibrium location of a segment is Δy. Equation (26) is the steady state of this compliance force. The mass for each segment is 500. The equilibrium radius is $a_0=9.5$ for $p_0=1/3$. Initially the tube has a constant radius a_0. The pressure p_s at each segment of the physical boundary is obtained by linear extrapolation. p_s-p_0 determines the net hydrodynamic force acting on this segment. The sum of the net hydrodynamic force and the compliance force gives the velocity and its displacement for each segment from the equilibrium location by Newtonian dynamics.

The radius and the pressure for part of the tube for steady flow are shown in Figs. 14 and 15 respectively. It is clear that the simulation results are in excellent agreement with the analytical predictions. In our numerical simulation, $\alpha=0.002, \tau=1, p(0)=0.297\,62$, and $p(L)=0.302\,94$. It should be noted that although we have obtained similar results in our previous paper [18], the present scheme reaches much higher accuracy.

B. Unsteady flow in artery

In the fluid domain, the continuity equation for the incompressible fluid reads

$$\nabla\cdot\mathbf{u}=0,$$

where $\mathbf{u}=\{u,v\}$ is the velocity of the fluid. The continuity equation can be written in terms of u and v as

$$\frac{\partial u}{\partial x}+\frac{\partial v}{\partial y}=0. \tag{29}$$

Integrating y from $y=-R$ to $y=R$, where R is the radius of the tube at x, we obtain

$$\frac{\partial}{\partial x}\int_{-R}^{R}u\,dy+v\big|_{-R}^{R}=0. \tag{30}$$

Recalling the symmetry of the tube

$$v_b=v\big|_{y=R}=-v\big|_{y=-R}, \tag{31}$$

one has

$$v_b=-R\frac{\partial u_m}{\partial x}, \tag{32}$$

where v_b is the radial velocity of the upper tube boundary and u_m is the average velocity of u, defined by

$$u_m=\frac{1}{a(x)}\int_{-R}^{R}u\,dy. \tag{33}$$

In Fig. 16 we show an example for simulation results. The pipe used is 200 lattice units in length and 38 lattice units in width when the pressure is fixed to be $p_0=0.333\,333\,3$ in the tube. In the simulation, the pressure at the outlet is fixed to be p_0, while the pressure at the inlet varies according to the equation

$$p_{inlet}=p_0+p_a\cos(\omega t), \tag{34}$$

where $\omega=2\pi/750$. The maximal velocities for the open and filled circles are 0.08 and 0.008, respectively. p_a is deter-

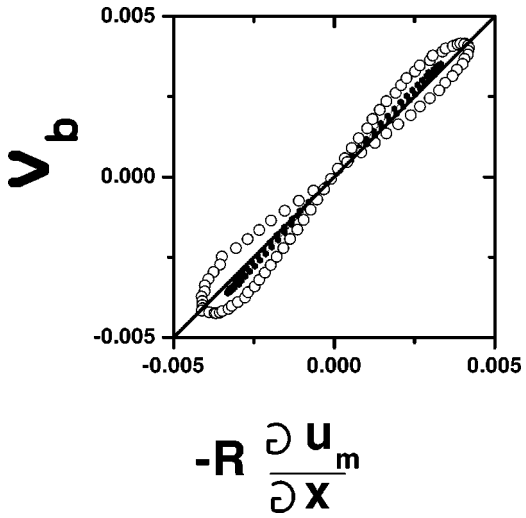

FIG. 16. v_b vs $-R\partial u_m/\partial x$ in an elastic tube with pulsatile fluid flow in a period at $x=10$. The maximal velocities in the tube for the open and filled circles are 0.08 and 0.008, respectively.

mined by the maximal velocity. The simulation results agrees with Eq. (32) approximately. The error results from the compressibility error of the lattice Boltzmann model. It is clear that the smaller the maximal velocity, the smaller the error. In the LBM, the continuity equation is Eq. (4), which is not incompressible. It seems that an incompresible model [20,21] is important to obtain accurate numerical results for the viscous flow in distensible blood vessels.

Finally we present our simulation results on the pulsatile flow in large blood vessels. The pipe is $L=1200$ units in length and 76 units in width initially with both sides closed. At discrete time $t=T,2T,\ldots,nT,\ldots,$ 1/500 of the total fluid particles in the pipe are injected into the pipe from the left side and ejected out of the pipe from the right side simultaneously with $T=671$. The fluid will then flow from left to right. Figures 17(a,b) display the typical flow field in the distensible blood vessel at $x=40$ of the tube. We find that both the axial velocity profiles and the centerline velocity wave are quite similar to the experimental results for the aortic flow (Fig. 7.27 of [2]). Considering that the simulation is performed in two dimensions while the experiment is in three dimensions with a viscoelastic blood wall, the agreement between our simulation results and the experimental ones [2] is rather satisfactory. We also show the radial velocity of the vessel wall in Fig. 17(c), the difference between the experiment and theoretical simulation results from the viscoelastic property of the wall. In the simulation, the tube wall is pure elastic so that the wave of the radial velocity is close to a sine function. The viscoelastic property of the blood wall leads to a simple pulse in the wave of the radial velocity from experiment.

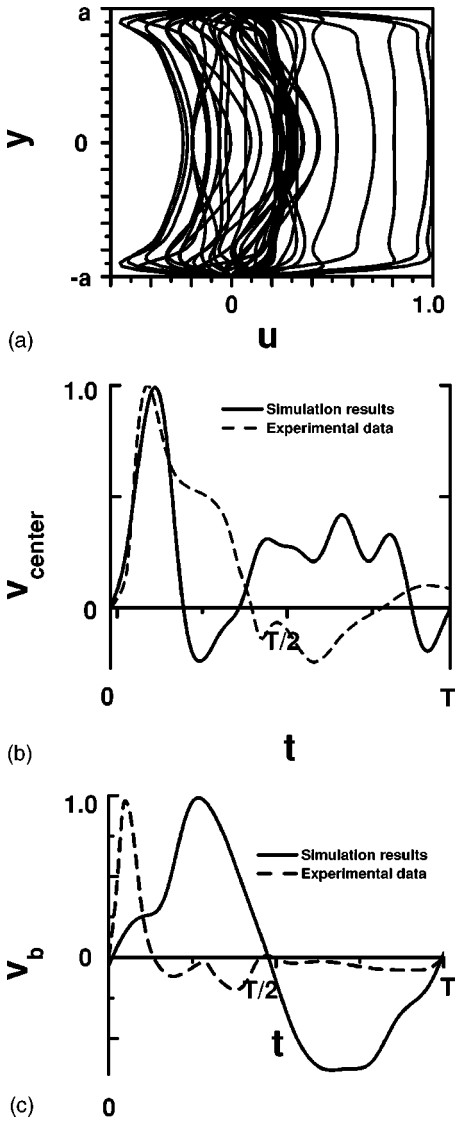

FIG. 17. The flow field in an elastic vessel at $x=40$. (a) The axial velocity profiles at different values of time t, (b) the centerline velocity wave, (c) the radial velocity of the vessel wall with respect to time t. The dashed lines in (b) and (c) are the experimental results for the aortic flow.

VI. CONCLUSION AND DISCUSSION

We have established a lattice Boltzmann model for simulating the viscous flow in large distensible blood vessels by introducing a boundary condition for elastic and moving boundaries. The mass conservation for the boundary condition is tested in detail, showing that the boundary condition can be used to study the flow with impermeable boundaries. The viscous flow in elastic vessels is simulated with the pressure-radius relationship similar to that of the pulmonary blood vessels. The numerical results for steady flow agree with the analytical prediction to very high accuracy, and the simulation results for pulsatile flow are favorable with that of the aortic flows observed experimentally. These results, together with the simplicity and the ease of implementation of the model, suggest that our approach may be a promising tool in studying the blood flow in arteries, especially in the diseased ones that suffer from atherosclerosis, stenosis, or aneurysm.

It should be noted that the compressibility of the model results in considerable error when pressure variation is large enough. Incompressible LBM models with explicit (nearly)

constant density are necessary to obtain accurate numerical results for the viscous flow in distensible blood vessels. Moreover, the blood wall is viscoelastic and blood is a viscoelastic fluid. It had been shown that the error of the elastic property of blood can be neglected when we only consider the flow in large blood vessels [2]. However, the viscoelstic behavior of the blood wall is important. We are working on this direction.

ACKNOWLEDGMENT

This work was supported by NSFC through Project Nos. 19704003, 19834070, and 19904004.

[1] Y.C. Fung, *Biomechanics Circulation* (Springer-Verlag, Berlin, 1997).
[2] T.J. Pedley, *The Fluid Mechanics of Large Blood Vessels* (Cambridge University Press, Cambridge, 1980).
[3] Y.H. Qian, D. d'Humiéres, and P. Lallemand, Europhys. Lett. **17**, 479 (1992).
[4] S. Chen, H. Chen, D.O. Martinez, and W.H. Matthaeus, Phys. Rev. Lett. **67**, 3776 (1991).
[5] U. Frisch, B. Hasslacher, and Y. Pomeau, Phys. Rev. Lett. **56**, 1505 (1986).
[6] D.H. Rothman and Zaleski, Rev. Mod. Phys. **66**, 1417 (1995).
[7] A.K. Gunstensen, D.H. Rothman, and Zaleski, and G. Zanetti, Phys. Rev. A **43**, 4320 (1991).
[8] X. Shan and H. Chen, Phys. Rev. E **47**, 1815 (1993); H.P. Fang *et al.*, Int. J. Mod. Phys. B **15**, 1287 (2001).
[9] M.R. Swift, E. Orlandini, W.R. Osborn, and J.M. Yeomans Phys. Rev. E **54**, 5041 (1996).
[10] A.J.C Ladd, J. Fluid Mech. **271**, 285 (1994).
[11] C.K. Aidun, Y. Lu, and E. Ding, J. Fluid Mech. **373**, 287 (1998).
[12] S.P. Dawson, S. Chen, and G. Doolen, J. Chem. Phys. **98**, 1514 (1993).
[13] H.W. Xi and C. Duncan, Phys. Rev. E **59**, 3022 (1999).
[14] C.H. Sun, Phys. Rev. E **58**, 7283 (1998).
[15] Z.F. Lin and H.P. Fang (unpublished).
[16] S.Y. Chen, D. Matinez, and R.W. Mei, Phys. Fluids **8**, 2527 (1996).
[17] O. Filippova and D. Hanel, Comput. Fluids **26**, 697 (1997).
[18] H.P. Fang, Z.F. Lin, and Z.W. Wang, Phys. Rev. E **57**, R25 (1998).
[19] D.P. Ziegler, J. Stat. Phys. **71**, 1171 (1993).
[20] H. P. Fang, R. Z. Wan, and Z. F. Lin (unpublished).
[21] X. He and L. Luo, J. Stat. Phys. **88**, 927 (1997).